# Supporting Information

## Solvent-free rapid synthesis of porous CeWO$_x$ by mechanochemical self-assembly strategy for the abatement of NO$_x$

Jixing Liu[1,2], Huifang Cheng[4], Junbin Tan[2], Bing Liu[3,*], Zihao Zhang[5], Haidi Xu[6], Minjie Zhao[2], Wenshuai Zhu[1], Jian Liu[2,*], Zhen Zhao[2]

[1] School of Chemistry and Chemical Engineering, Institution for Energy Research, Jiangsu University, Zhenjiang 212013, PR China;

[2] State Key Laboratory of Heavy Oil and Beijing Key Lab of Optical Detection Technology for Oil and Gas, China University of Petroleum, Beijing 102249, People's Republic of China;

[3] Department of Chemical Engineering, School of Chemical and Material Engineering, Jiangnan University, Wuxi 214122, People's Republic of China;

[4] College of Material Science and Engineering, Hebei University of Engineering, Handan 056038, Hebei, People's Republic of China;

[5] Pacific Northwest National Laboratory, Richland, WA 99352, USA;

[6] Institute of New Energy and Low-Carbon Technology & College of Chemistry, Sichuan University, Chengdu 610065, China

*Correspondence and requests for materials should be addressed to B.L. (E-mail: liubing@jiangnan.edu.cn), and J.L. (E-mail: liujian@cup.edu.cn)

**1.1. Catalysts characterization.** The texture properties of various $CeWO_x$ oxides were detected by the $N_2$ adsorption-desorption isotherm performed on Micromeritics Tristar II 3020 porosimetry analyzer at −196 °C. The microstructure of $CeWO_x$ catalysts was conducted on a JEOL JEM LaB6 2100 electron microscope. The crystal phase structures of these catalysts were carried out by X-ray diffraction (XRD, Shimadzu X-6000). Surface chemical valence state was investigated by X-ray photoelectron spectra (XPS) carried out on a PerkinElmer PHI-1600 ESCA spectrometer. Hydrogen ($H_2$) temperature-programmed reduction ($H_2$-TPR) and ammonia temperature-programmed desorption ($NH_3$-TPD) experiments were conducted on a USA Quantachrome apparatus. Prior to each data acquisition, the samples (100 mg) were pretreated from room temperature to 400 °C at a rate of 10 °C min$^{-1}$ and then cooled to 60 °C in a pure $N_2$ flow. The adsorption properties of $NH_3$ and $NO_x$ were probed by *in-situ* diffuse reflection fourier transform infrared spectroscopy (DRIFTS) on a Nicolet IS50 FT-IR spectrometer. Prior to each experiment, the samples were first purged in flowing $N_2$ at 400 °C for 1 h.

**1.2 DFT calculations.** All the spin-polarized density functional theory (DFT) calculations were performed by using the Vienna *ab initio* simulation package (VASP).[1,2] To accurately treat the highly localized Ce4f-orbitals, we conducted DFT+U calculations with a value of $U_{eff}$ = 5.0 eV applied to the Ce4f states.[3] The D3 correction method (DFT-D3) was employed in order to include van der Waals (vdW) interactions.[4] The projector-augmented wave (PAW) method was used to represent core-valence interactions.[5] Valence electrons were described by a plane wave basis with an energy cutoff of 400 eV. The generalized gradient approximation with the Perdew-Burke-Ernzerhof (GGA-PBE) functional was used to model electronic exchange and correlation.[6] Electron smearing was employed via Gaussian smearing method with a smearing width consistent to 0.05 eV. The conjugate gradient algorithm was used in the geometry optimization calculations. Optimized structures were obtained by minimizing the forces on each ion until they were less than 0.03 eV/Å. The Brillouin zone was sampled at the Γ-point. Transition states (TSs) for the elementary reactions were located using the climbing-image nudged elastic band (CI-NEB) method,[7,8] and were confirmed as having a single imaginary frequency. The activation barrier ($E_a$) was calculated as the energy difference between the transition and initial states.

The adsorption energy ($E_{ads}$) is defined as:[9,10]

$$E_{ads} = E(adsorbate + surface) - E(adsorbate) - E(surface)$$

where E(adsorbate + surface) is the total energy of the adsorbate interacting with the surface; E(adsorbate) and E(surface) are the energies of the free adsorbate in gas phase and the bare surface, respectively. A negative value corresponds to exothermic adsorption, with more negative values corresponding to stronger binding.

The oxygen vacancy formation energy ($E_{vac}$) was defined as:[11]

$$E_{vac} = E(surface_{vac}) + \frac{1}{2}E(O_2) - E(surface)$$

Where $E(surface_{vac})$ and E(surface) are the total energies of the optimized surface with and without an oxygen vacancy, respectively, and $E(O_2)$ is the energy of the gas-phase $O_2$ molecule. A positive $E_{vac}$ value indicates that extra energy is needed to create the vacancy.

**Table S1**. Calculated DFT energy values for $W_1$-$CeO_2$(111), $W_2$-$CeO_2$(111), $W_3$-$CeO_2$(111), and pure $CeO_2$(111) surfaces.

| Surface | $E_{surface}$ (eV) | $E_{surface-vac}$ (eV) |
|---|---|---|
| $W_1$-$CeO_2$(111) | -882.41844468 | -876.22265557 |
| $W_2$-$CeO_2$(111) | -888.05523880 | -882.28992006 |
| $W_3$-$CeO_2$(111) | -893.64495017 | -887.37518530 |
| Pure $CeO_2$(111) | -877.04563603 | -869.65730503 |

The surface energy of $W_1$-$CeO_2$(111), $W_2$-$CeO_2$(111), and $W_3$-$CeO_2$(111) was calculated based on equation (1):

$$\gamma = \frac{1}{2A}\left[E_{slab}(W_mCe_{n-m}O_{2n}) - (n-m)E_{bulk}(CeO_2) - mE_{bulk}(W) - 2m\mu_O(T,P)\right] \quad (1)$$

Where $E_{slab}(W_mCe_{n-m}O_{2n})$ is the DFT calculated energy of W-doped $CeO_2$(111) structure, $E_{bulk}(CeO_2)$ and $E_{bulk}(W)$ represent the DFT calculated energy of bulk $CeO_2$ and W, respectively, $A$ is the surface area of the slab model, and $\mu_O(T,P)$ is the chemical potential of oxygen atom, which was calculated using equation (2):

$$\mu_O(T,P) = \frac{1}{2}[E_{O_2} + \Delta\mu_{O_2}(T,P)] \quad (2)$$

Where $E_{O_2}$ is DFT calculated energy of gas-phase oxygen molecule, and $\Delta\mu_{O_2}(T,P)$ can be obtained on

the NIST website.

Accordingly, we can obtain the surface energy of $W_1$-$CeO_2$(111), $W_2$-$CeO_2$(111), and $W_3$-$CeO_2$(111) at T = 298.15 K and P = 1 atm. The results are listed in the following Table.

**Table S2**. Calculated surface energy of $W_1$-$CeO_2$(111), $W_2$-$CeO_2$(111), and $W_3$-$CeO_2$(111) surfaces.

| Surface | Surface energy $\gamma$ (J/m$^2$) |
|---|---|
| $W_1$-$CeO_2$(111) | 0.83 |
| $W_2$-$CeO_2$(111) | 0.49 |
| $W_3$-$CeO_2$(111) | 0.14 |

The computational model of $W_3$-$CeO_2$(111) was constructed by using three W atom to replace three surface Ce atom in pure $CeO_2$ model, as shown in **Fig. S1(a)** and **S1(b)**. After geometric optimization, we obtained the $W_3$-$CeO_2$(111) structural model. It can be seen that there is obvious structure transformation for $W_3$-$CeO_2$(111) doped model in comparison with pure $CeO_2$. This is reasonable because W oxide has a different structure and coordination environment in comparison with ceria oxide and W-O bond length is shorter than Ce-O bond length. Therefore, after the introduction of three W dopants into $CeO_2$, the bond angle, bond length and coordination number of local structure neighboring W dopants are all changed and some Ce-O bonds are broken.
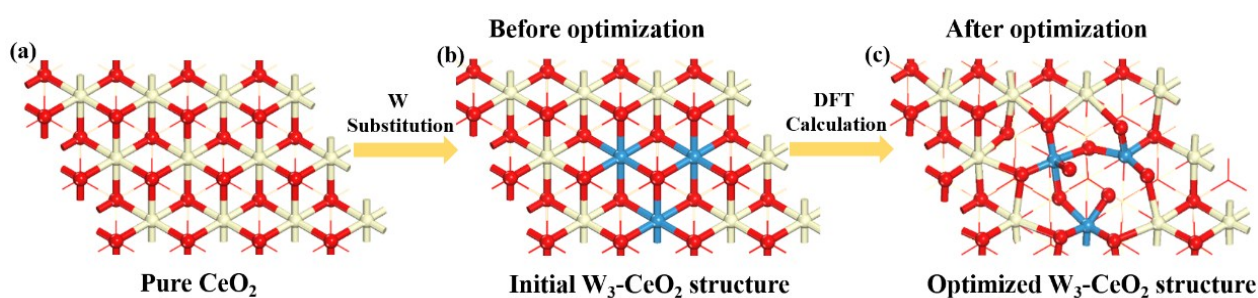


**Fig. S1** Illustration of the construction of $W_3$-$CeO_2$(111) computational model.

In our DFT calculations for $NH_3$ adsorption, we considered different adsorption sites for $NH_3$ on each W-doped $CeO_2$ surface, and **Fig. 6(j)**, 6(k), and 6(l) show the most favorable adsorption site for $NH_3$ on $W_1$-$CeO_2$(111), $W_2$-$CeO_2$(111), and $W_3$-$CeO_2$(111) surfaces, respectively. For $W_1$-$CeO_2$(111) surface, three adsorption site for $NH_3$ were calculated: W site, $Ce_1$ site, and $Ce_2$ site, as shown in the following **Fig. S2**. Comparing the adsorption energies at these three sites, it can be concluded that $NH_3$ adsorption at $Ce_1$ site is the most stronger and thus $Ce_1$ site is the most favorable

binding site for NH$_3$. While for W$_2$-CeO$_2$(111) and W$_3$-CeO$_2$(111) surfaces, W$_2$ site is the most favorable binding site for NH$_3$ due to the more negative adsorption energy. Therefore, the most favorable adsorption site for NH$_3$ on W$_1$-CeO$_2$(111) is different from that on W$_2$-CeO$_2$(111) and W$_3$-CeO$_2$(111). This is why **Fig. 6(j)** shows that NH$_3$ was located at Ce site for W$_1$-CeO$_2$ surface while **Fig. 6(k)** and **6(l)** show NH$_3$ was located at W site for W$_2$-CeO$_2$ and W$_3$-CeO$_2$ surfaces.
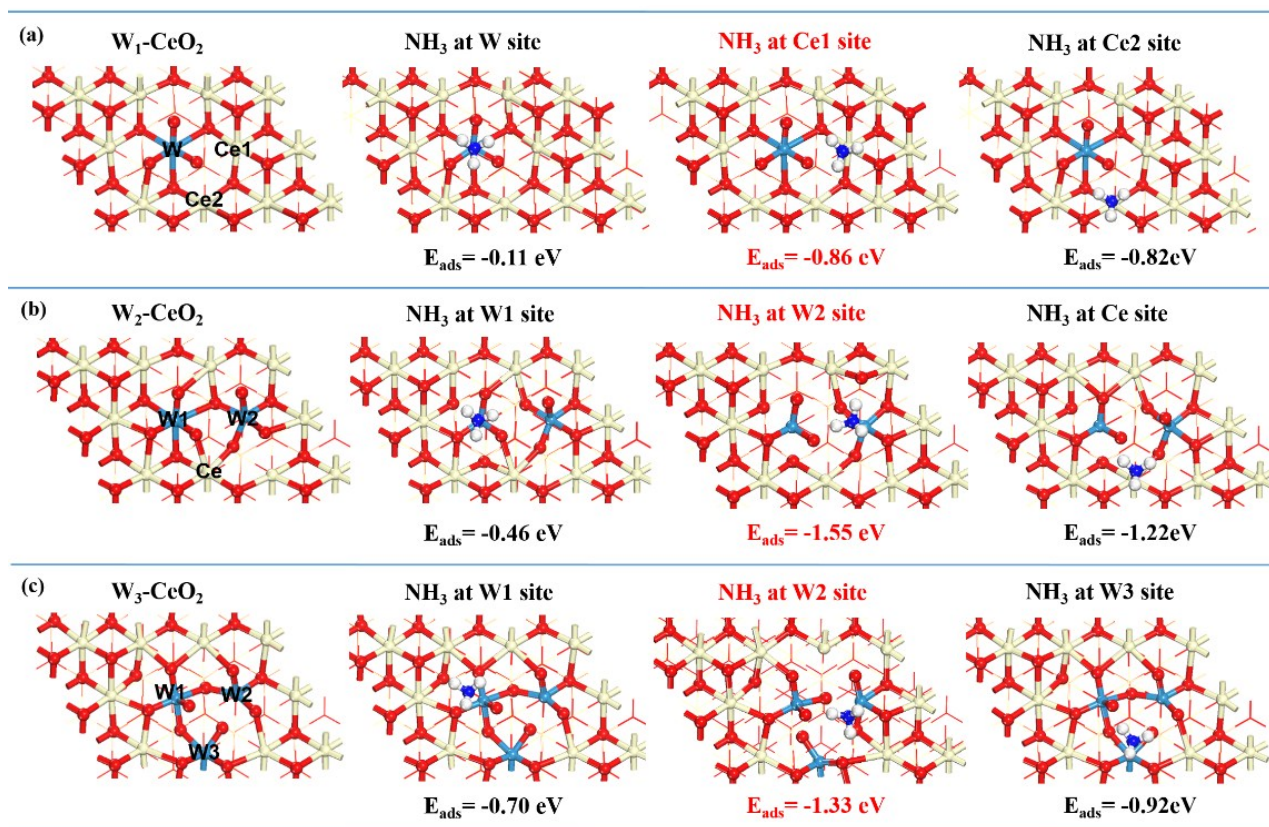


**Fig. S2** NH$_3$ adsorption at different adsorption sites for (a) W$_1$-CeO$_2$(111), (b) W$_2$-CeO$_2$(111), and (c) W$_3$-CeO$_2$(111) surfaces.

## Reference

1    G. Kresse and J. Furthmuller, *Phys. Rev. B*, 1996, **54**, 11169−11186.

2    G. Kresse and J. Furthmuller, *Comput. Mater. Sci.*, 1996, **6**, 15−50.

3    B. Liu, J. Liu, S. Ma, Z. Zhao, Y. Chen, X. Q. Gong, W Song, A. Duan and G. Jiang, *J. Phys. Chem. C*, 2016, **120**, 2271−2283.

4    S. Grimme, J. Antony, S. Ehrlich and H. Krieg, *J. Chem. Phys.*, 2010, **132**, 154104.

5    P. E. Blöchl, *Phys. Rev. B*, 1994, **50**, 17953−17979.

6   J. P. Perdew, K. Burke and M. Ernzerhof, *Phys. Rev. Lett.*, 1996, **77**, 3865−3868.

7   G. Henkelman and H. Jónsson, *J. Chem. Phys.*, 2000, **113**, 9978−9985.

8   G. Henkelman, B. P. Uberuaga and H. Jónsson, *J. Chem. Phys.*, 2000, **113**, 9901−9904.

9   B. Liu, Z. Zhao, G. Henkelman and W. Song, *J. Phys. Chem. C*, 2016, **120**, 5557−5564.

10  B. Liu, W. Li, Y. Xu, Q. Lin, F. Jiang and X. Liu, *ACS Catal.*, 2019, **9**, 7073−7089.

11  B. Liu, W. Li, W. Song and J. Liu, *Phys. Chem. Chem. Phys.*, 2018, **20**, 16045−16059.